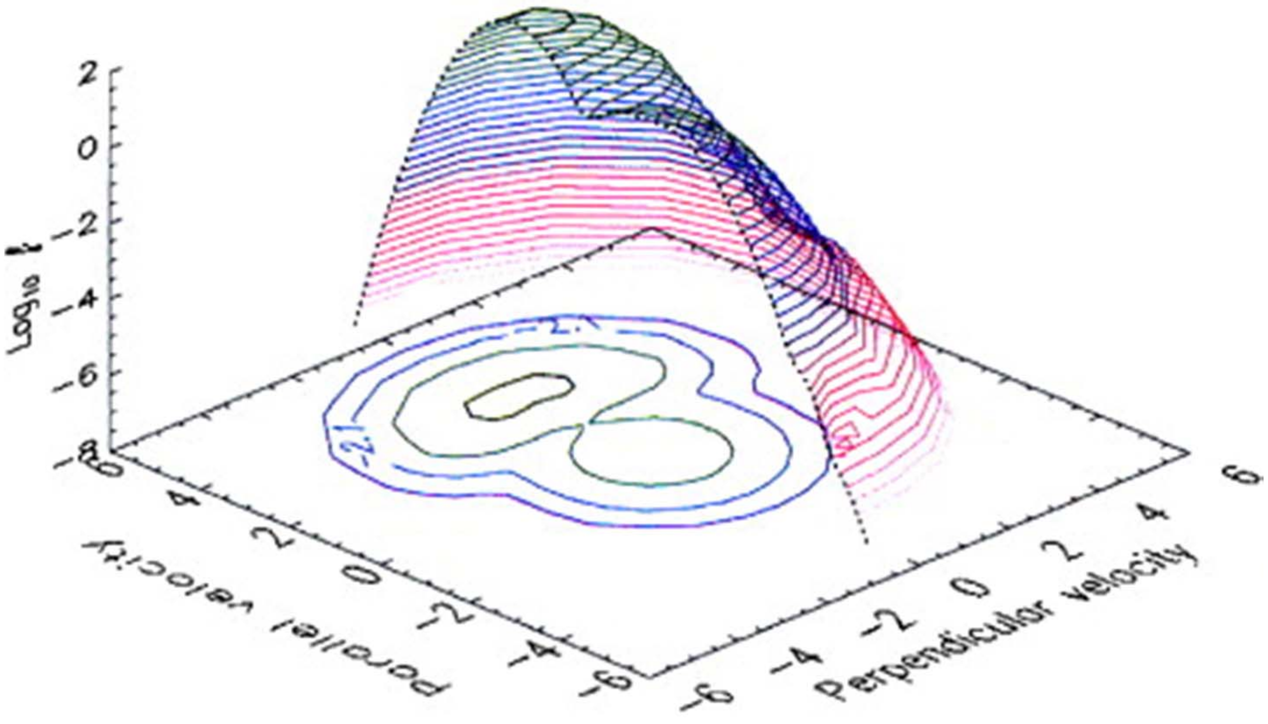

Velocity distribution function at 2000 km

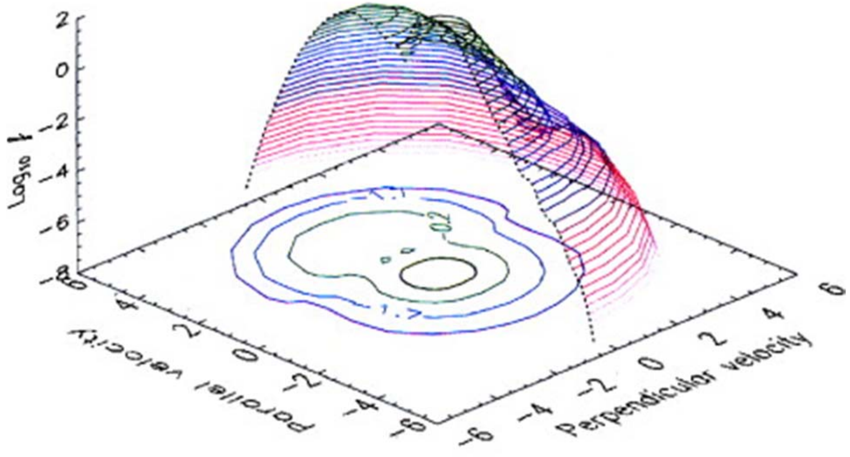

Velocity distribution function at 1250 km

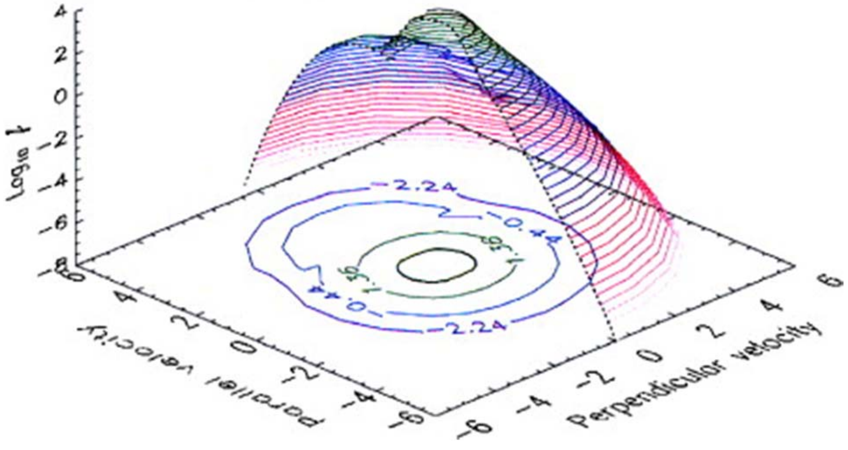

Velocity distribution function at 1000 km

http://origin-ars.els-cdn.com/content/image/1-s2.0-S1364682607002404-gr7.jpg

Electron velocity distribution function in the solar wind measured by Helios spacecraft at 1 AU.

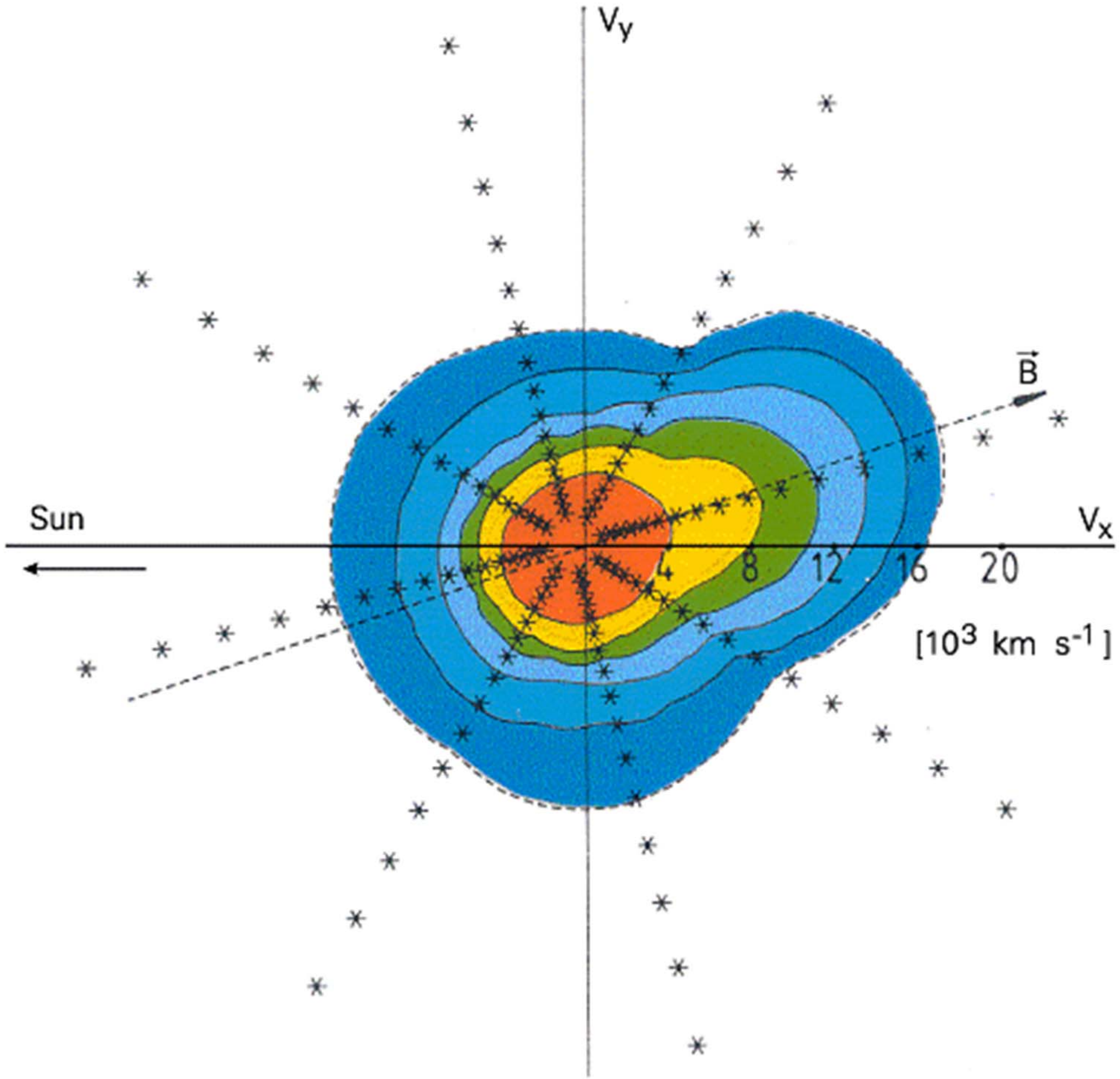

http://solarphysics.livingreviews.org/Articles/lrsp-2006-1/fig_1.html

Core
Maxwellian

Halo
Kappa

Strahl
Field Aligned
Beam

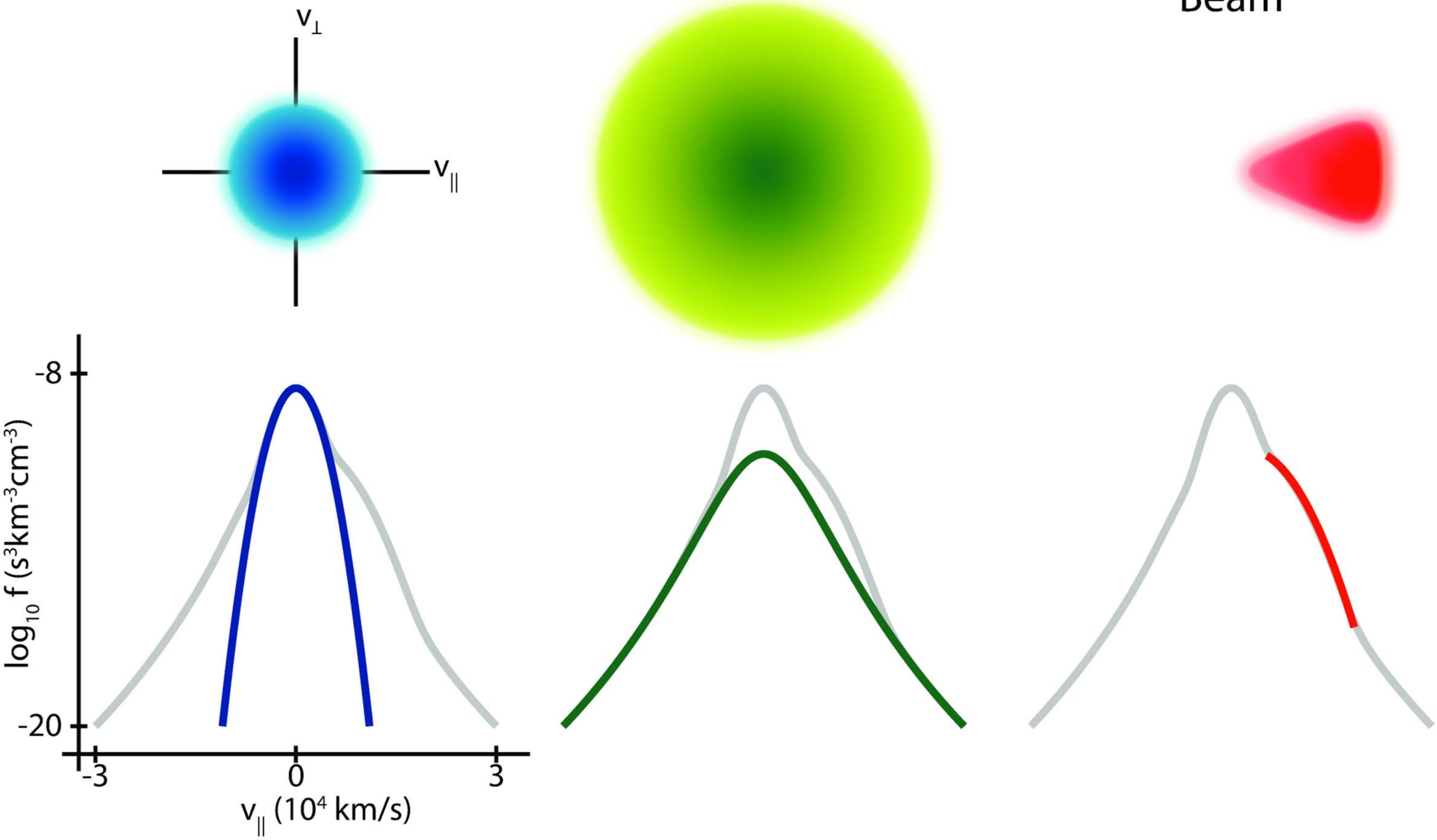

http://sprg.ssl.berkeley.edu/~pulupa/illustrations/electrons/elects.png

Electron velocity distribution functions for fast (left), intermediate (middle) and slow (right) solar wind.

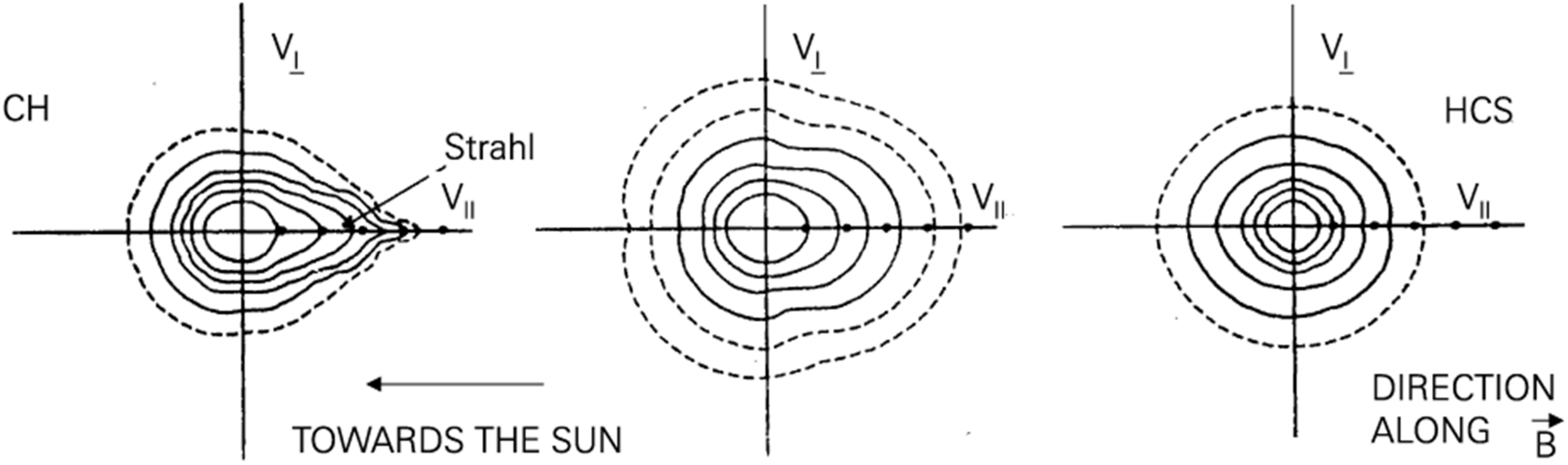

http://solarphysics.livingreviews.org/Articles/lrsp-2006-1/fig_2.html

Proton velocity distribution functions in the fast solar wind measured by Helios.

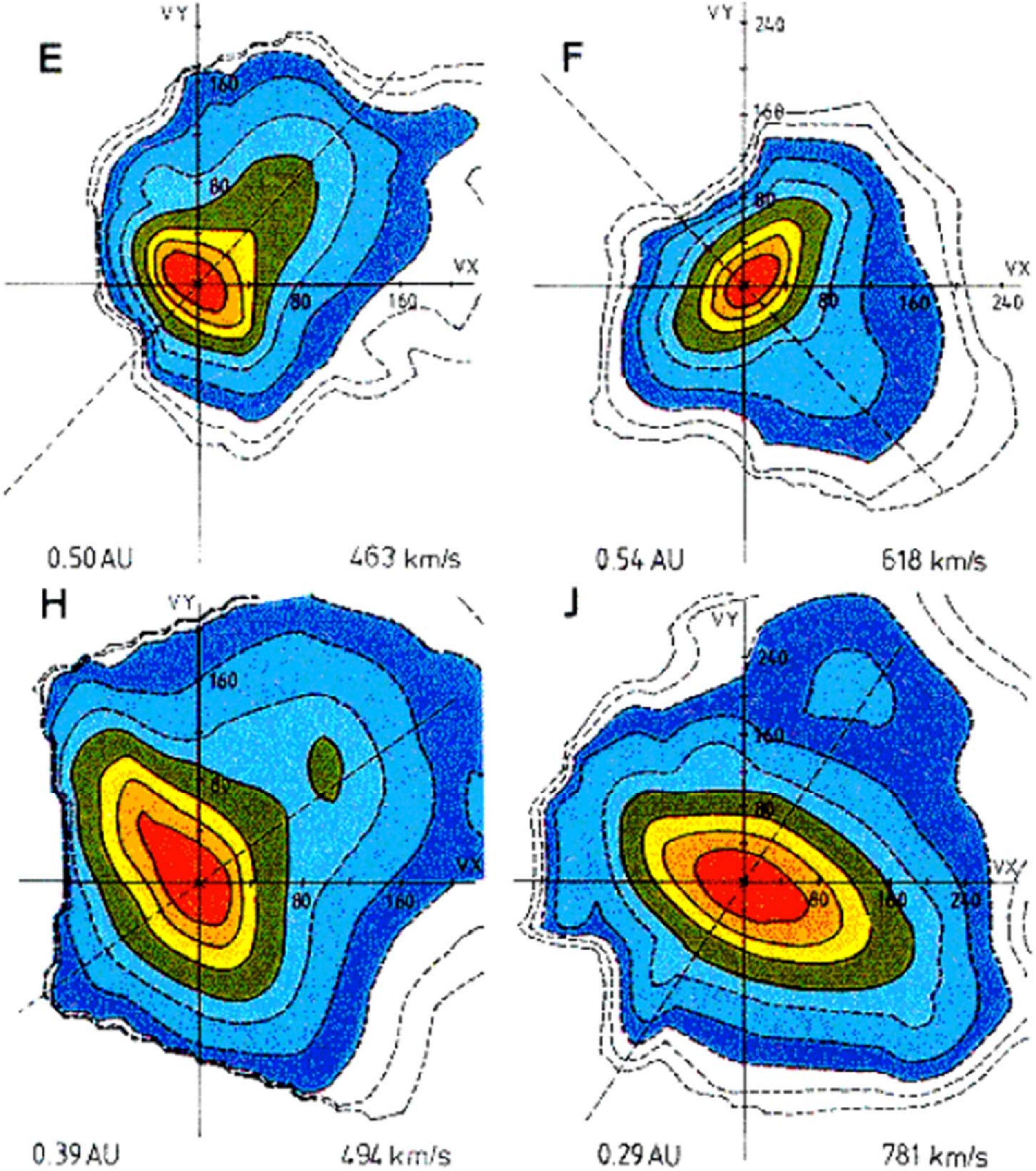

http://solarphysics.livingreviews.org/Articles/lrsp-2006-1/fig_3.html

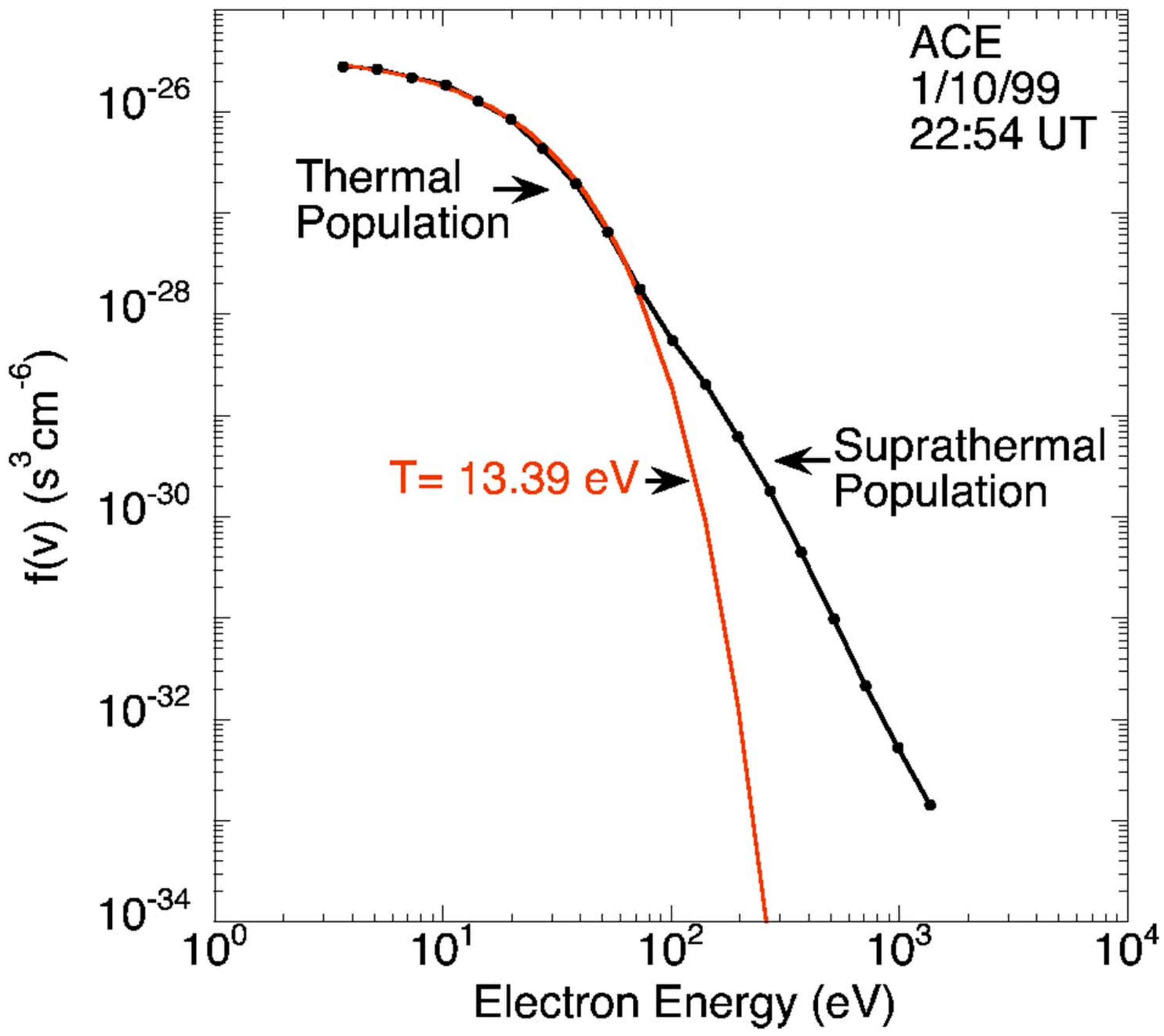

Measurements of electron energy distributions in the solar wind reveal the presence of both thermal and suprathermal populations.

“The Solar Wind” by J. T. Gosling, 2009

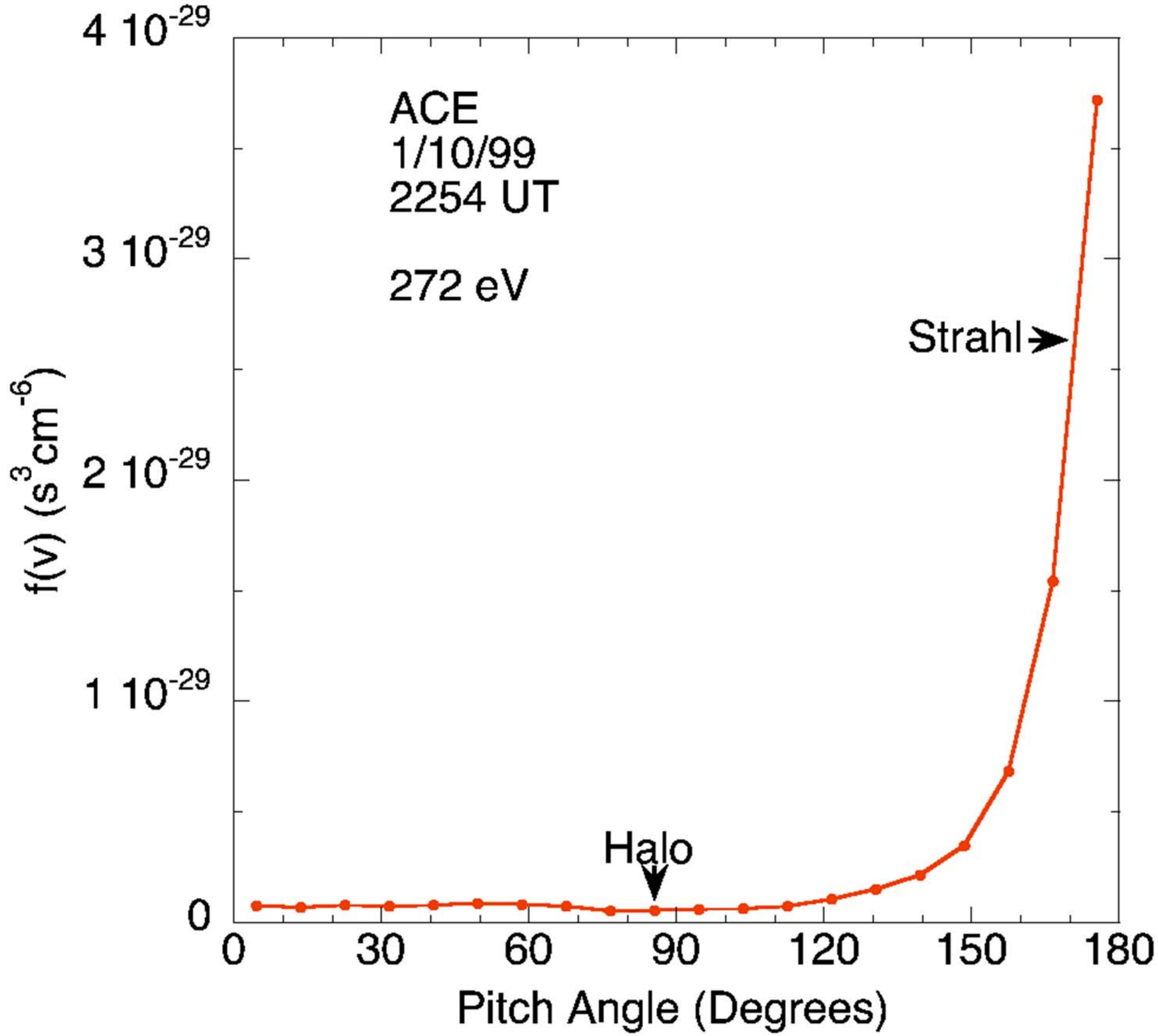

The suprathermal population is nearly collisionless, carries the solar wind heat flux, and includes both a field-aligned “strahl” (or beam) and a roughly isotropic “halo”.

“The Solar Wind” by J. T. Gosling, 2009

Counterstreaming Suprathermal Electrons as Tracers of Closed Magnetic Field Lines in CMEs

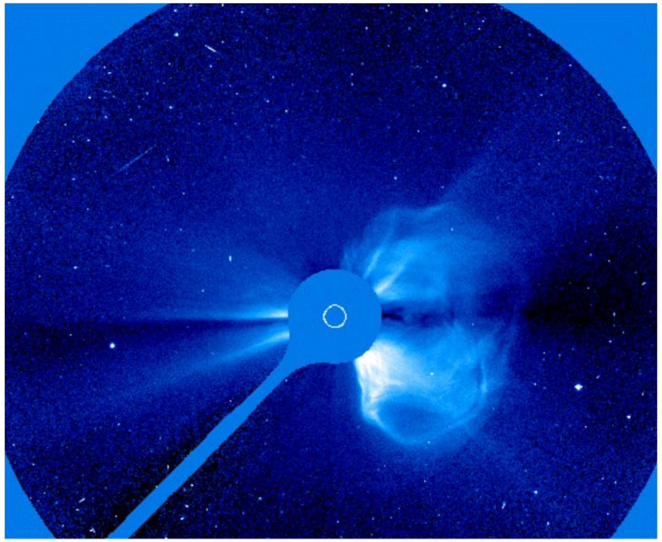

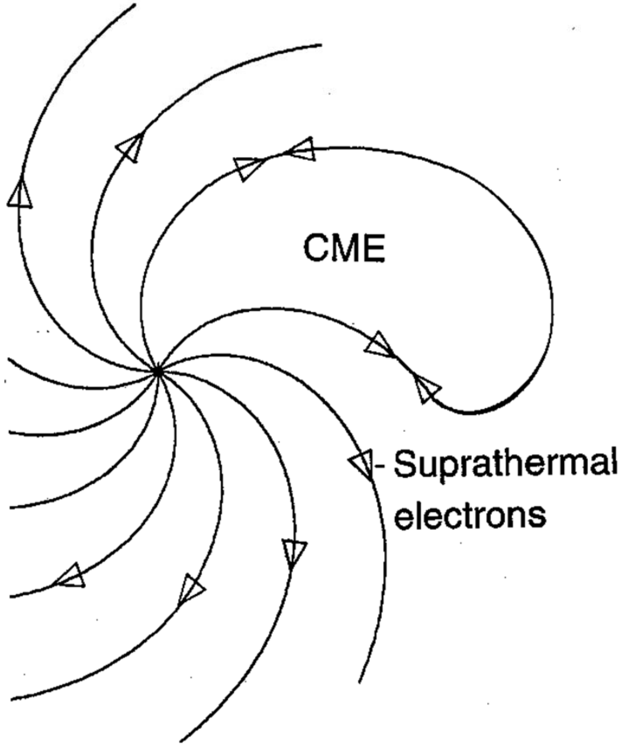

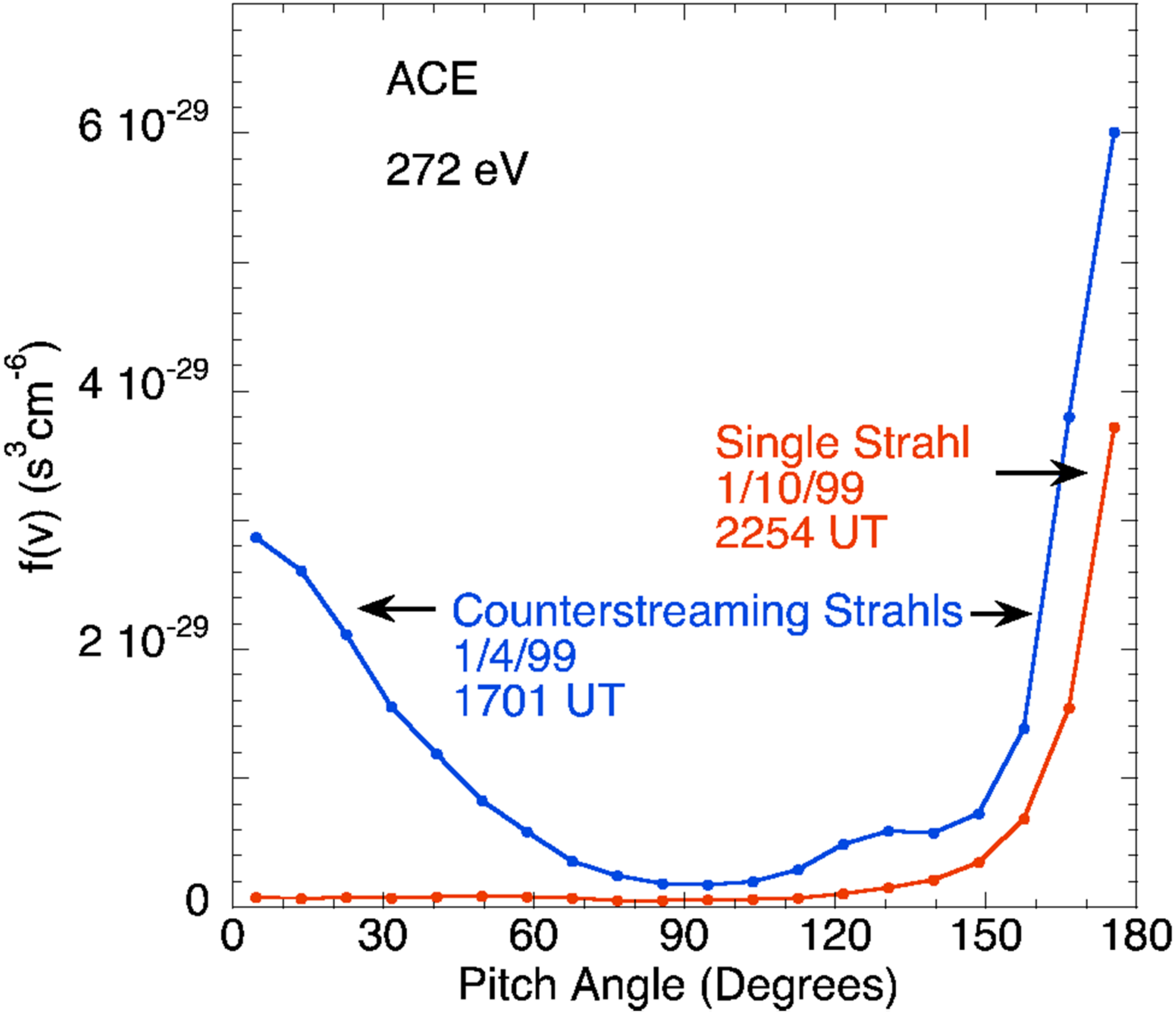

“The Solar Wind” by J. T. Gosling, 2009

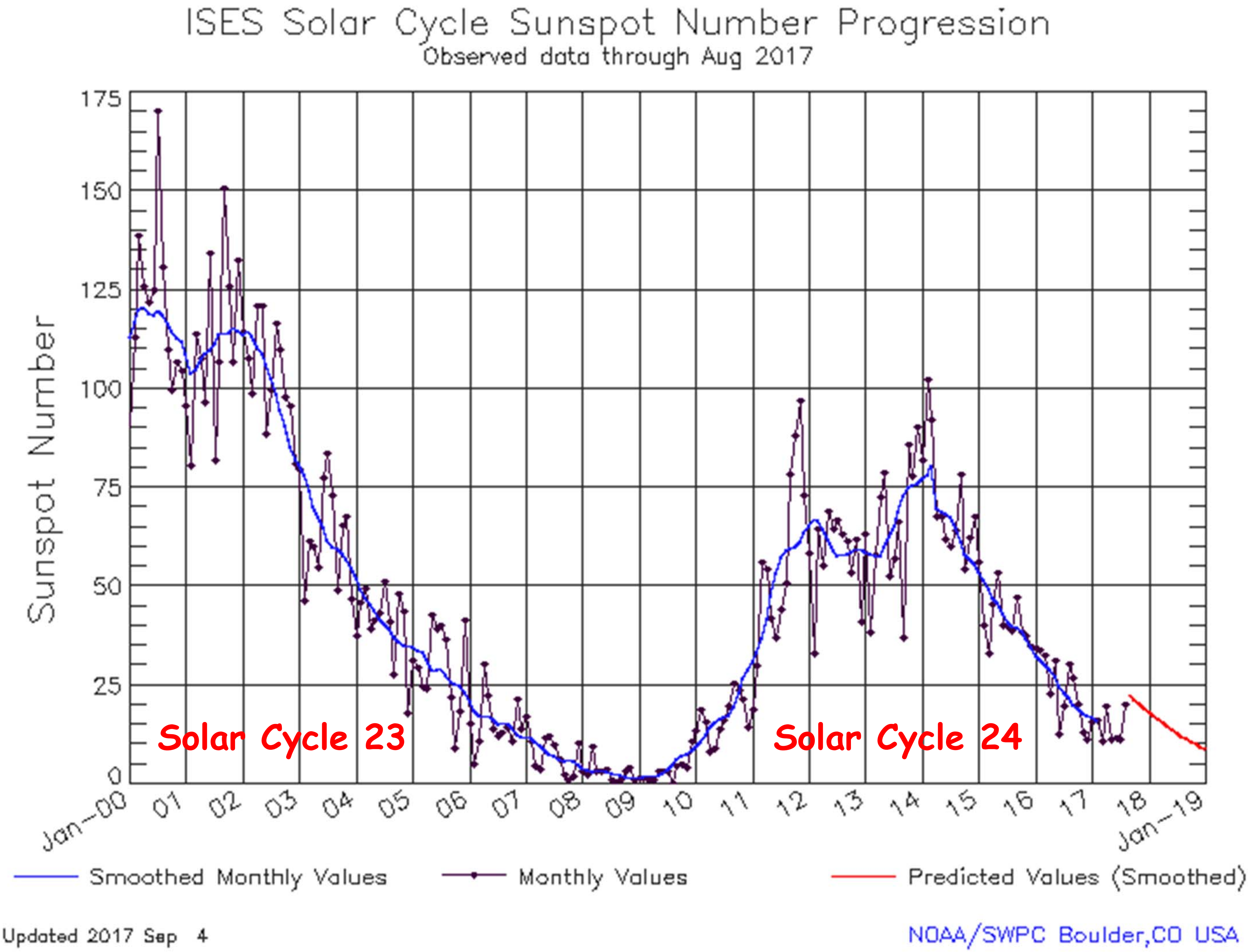

http://www.swpc.noaa.gov/products/solar-cycle-progression

Solar Cycle List

週期	開始	結束	時間（年）	極大期	太陽黑子極少的天數
1	1755/3	1766/6	11.3	1761/6	
2	1766/6	1775/6	9.0	1769/9	
3	1775/6	1784/9	9.3	1778/5	
4	1784/9	1798/5	13.6	1788/2	
5	1798/5	1810/12	12.3	1805/2	
6	1810/12	1823/5	12.8	1816/5	
7	1823/5	1833/11	10.5	1829/11	
8	1833/11	1843/7	9.7	1837/3	
9	1843/7	1855/12	12.4	1848/2	655
10	1855/12	1867/3	11.3	1860/2	406
11	1867/3	1878/12	11.8	1870/8	1028
12	1878/12	1890/3	11.3	1883/12	736
13	1890/3	1902/2	11.8	1894/1	934
14	1902/2	1913/8	11.5	1906/2	1023
15	1913/8	1923/8	10.1	1917/8	534
16	1923/8	1933/9	10.1	1928/4	568
17	1933/9	1944/2	10.4	1937/4	269
18	1944/2	1954/4	10.2	1947/5	446
19	1954/4	1964/10	10.5	1958/3	227
20	1964/10	1976/6	11.4	1968/11	272
21	1976/6	1986/9	10.5	1979/12	273
22	1986/9	1996/5	9.9	1989/11	309
23	1996/5	2008/12	12.3	2001/11	817
24	2008/12			2014/4	
平均數			11.04		

http://en.wikipedia.org/wiki/List_of_solar_cycles

Co-rotating Interaction Region (CIR)

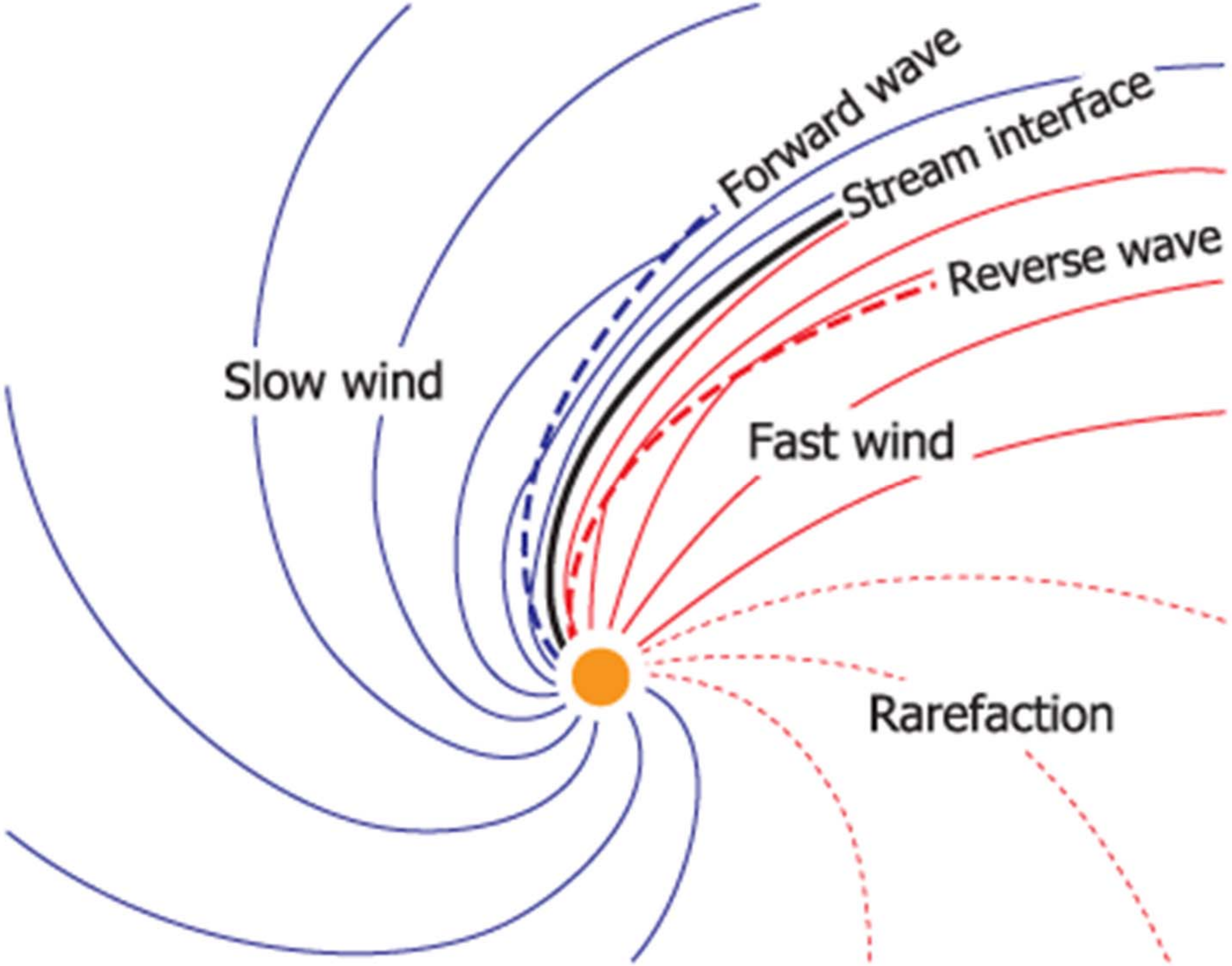

http://solarphysics.livingreviews.org/Articles/lrsp-2013-5/CIR_2panel.png

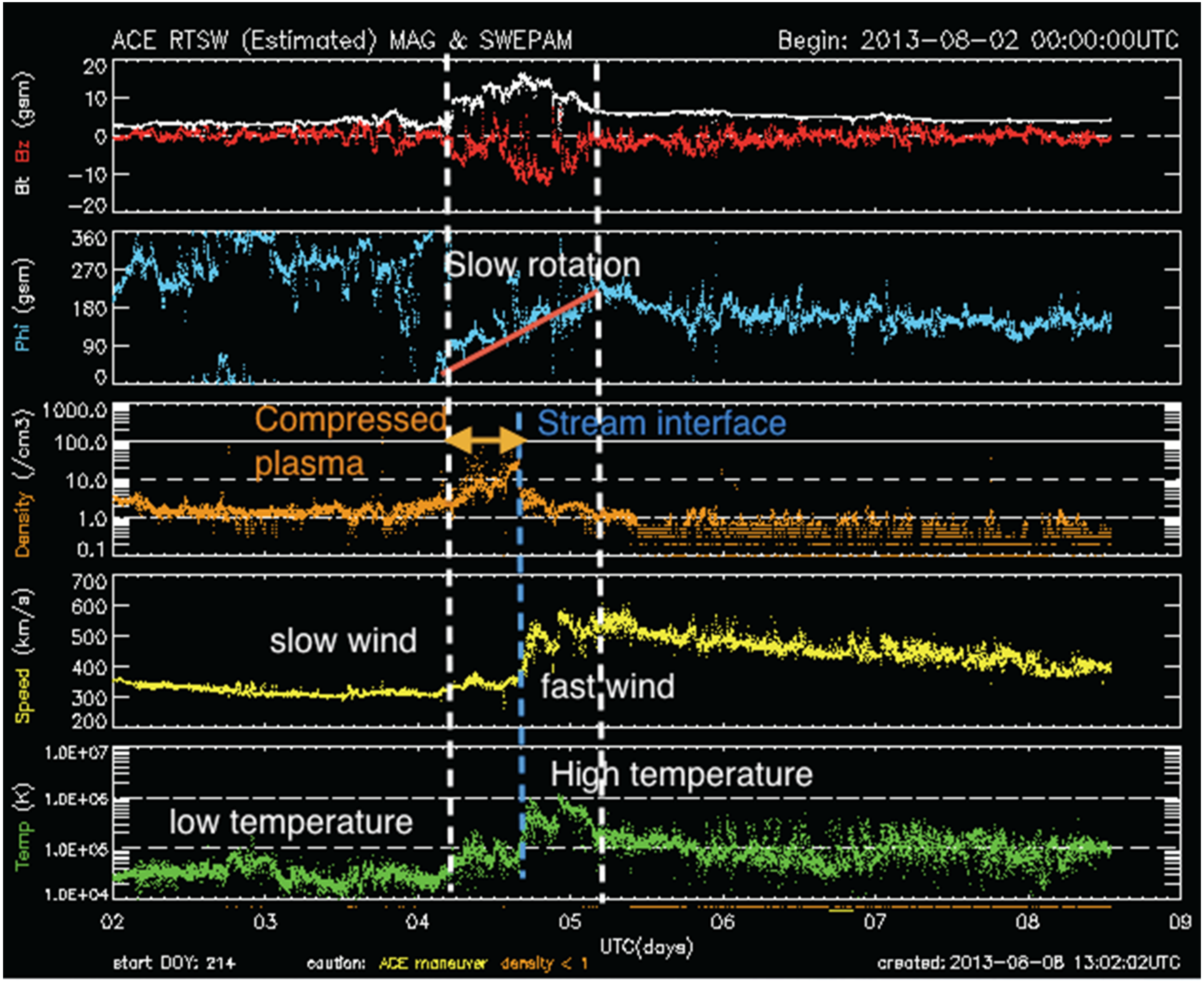

http://wis.kuleuven.be/CHARM/images/partners/20130919-eheroesschoolleuven.pdf

The CIR-associated increases cover around four orders-of-magnitude above background, but most surprisingly, they extend to the highest latitudes reached by Ulysses of just over 80°.

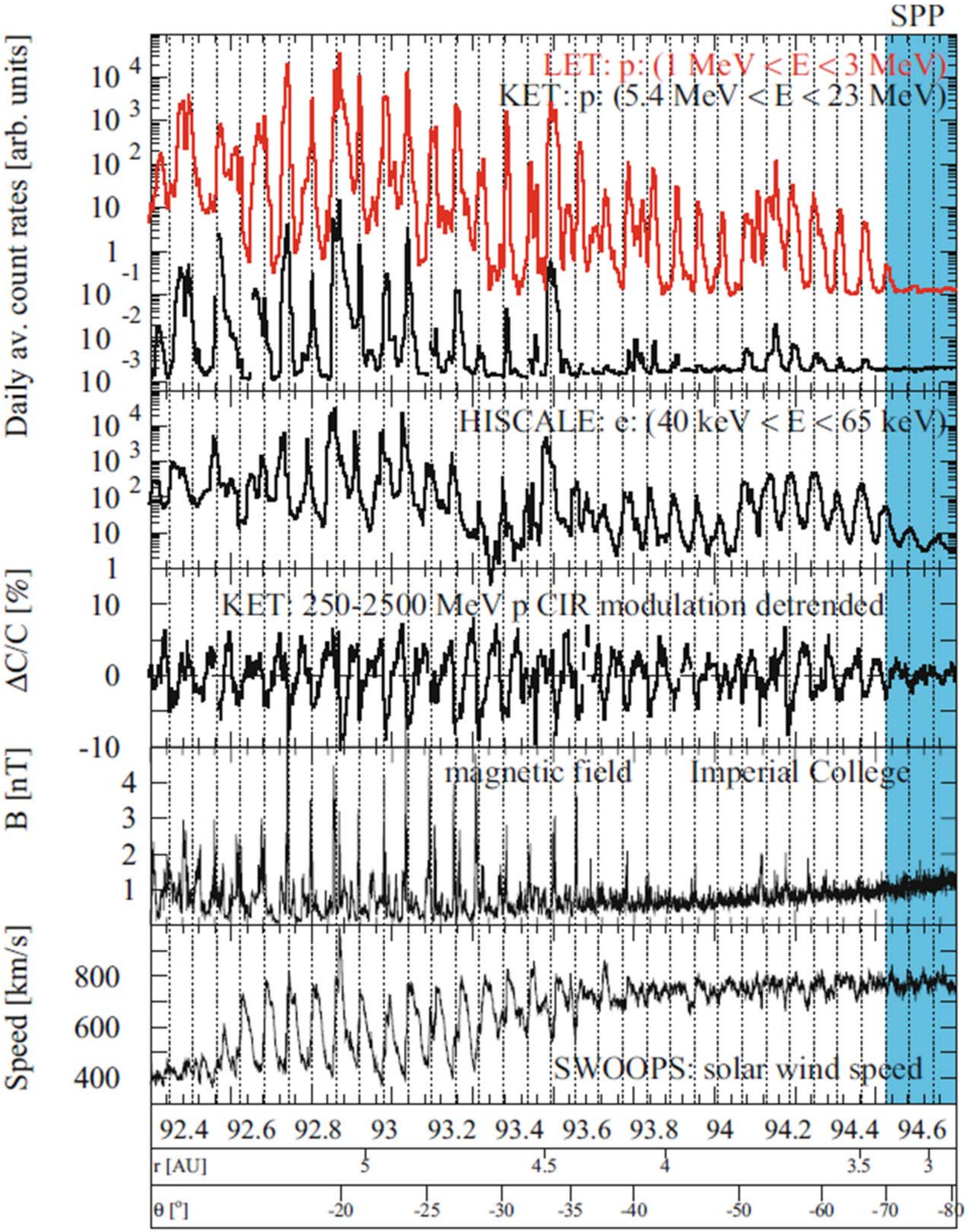

The amplitude of the CIR-induced changes cover almost five orders-of magnitude in intensity at times in the 1–3MeV region, with similar but less dramatic changes at slightly higher energies.

The peaks in the cosmic rays are anticorrelated with the peaks in the solar wind, indicating that the CIRs serve to exclude locally some of the high energy cosmic rays.

Fig. 6.3 (p.124) in Simnett et al. (2017)

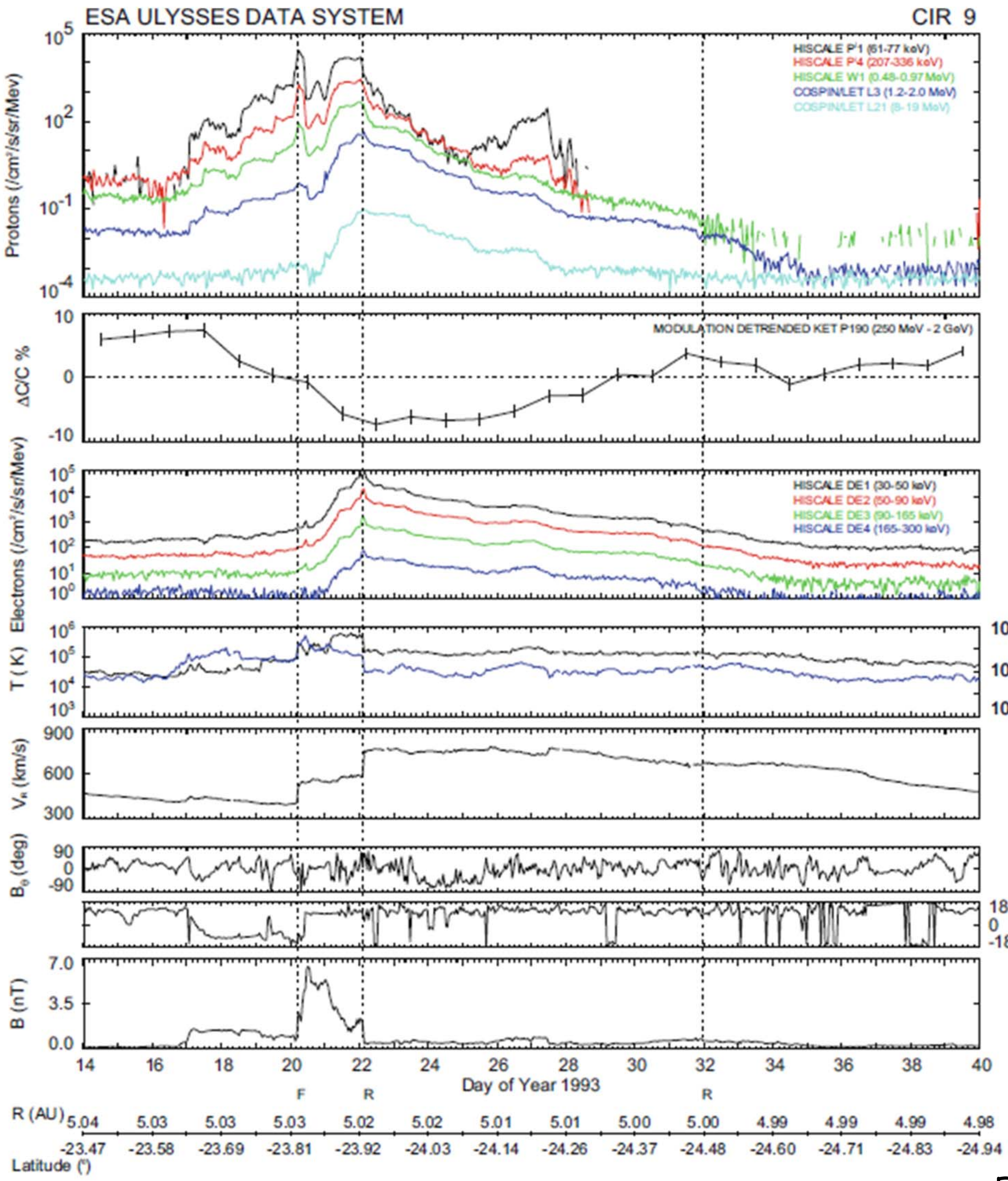

There are maxima in the ion intensity at both shocks. However, the energy spectrum is quite different at the two shocks. For the electrons, the intensity at the forward shock is little enhanced, but the reverse shock intensity is almost three orders-of-magnitude above the background. Careful examination reveals that the 1–3MeV proton intensity tends to fall to the background level faster than the 40–65 keV electrons. In other words, the CIR is more effective in influencing the background electron intensity in the whole of the inner heliosphere than it is for the protons. The CIR is effective in modulating the galactic cosmic rays, which are plotted in the second panel.

Fig. 6.4 (p.126) in Simnett et al. (2017)

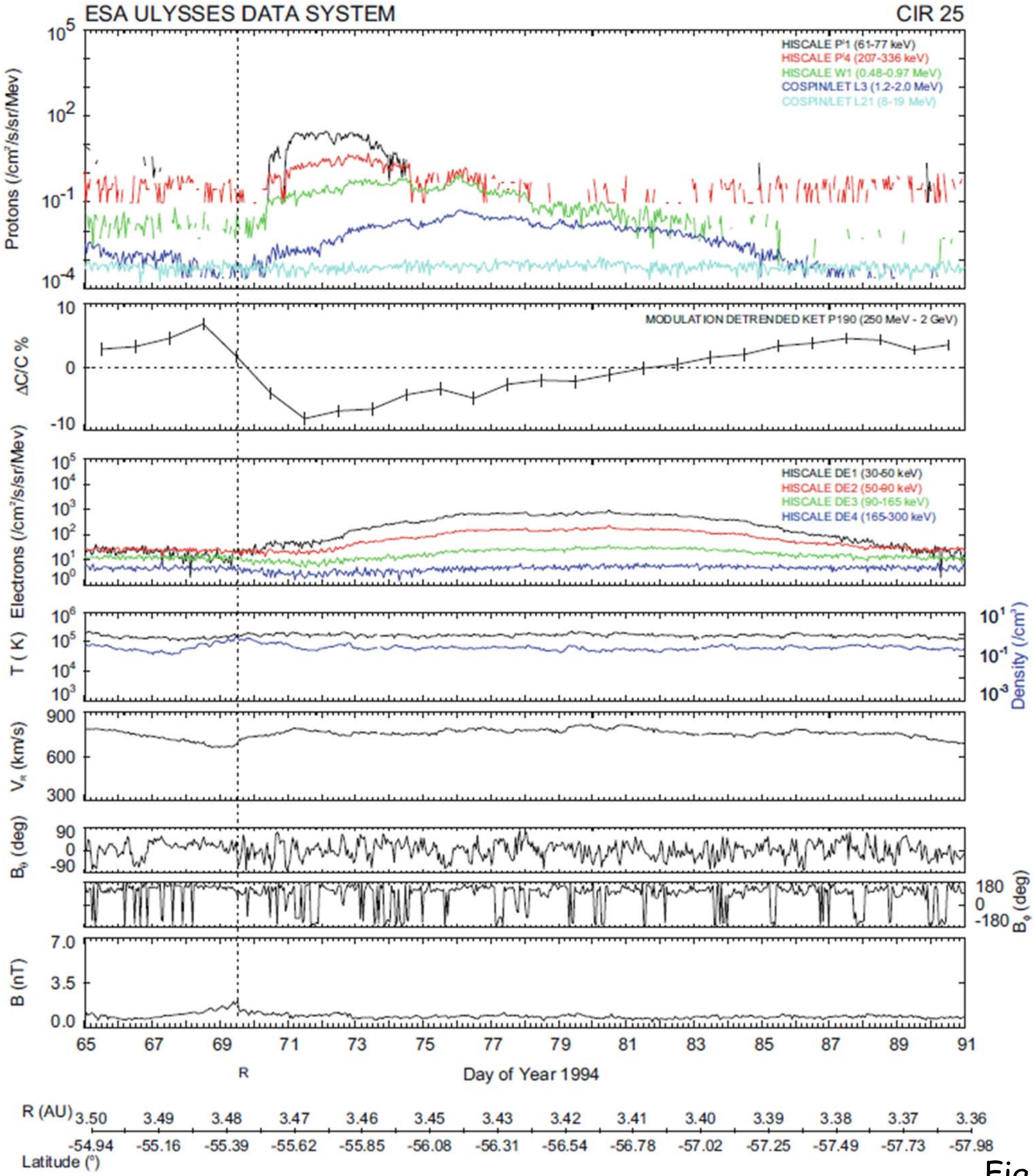

There is a small reverse “wave” seen on day 69. This is not accompanied by any increase in the energetic particle intensities at the time. However, about a day later there is an increase which is most pronounced at the lowest energy, but which reaches a maximum at progressively later times as the energy increases. The increase in the electrons becomes very broad in time, lasting well over half the solar rotation. The lag in the appearance of the higher energy/higher velocity particles can be explained as the consequence of remote magnetic connection of Ulysses at high latitudes to the CIRs that are present at low latitudes.

Fig. 6.5 (p.128) in Simnett et al. (2017)

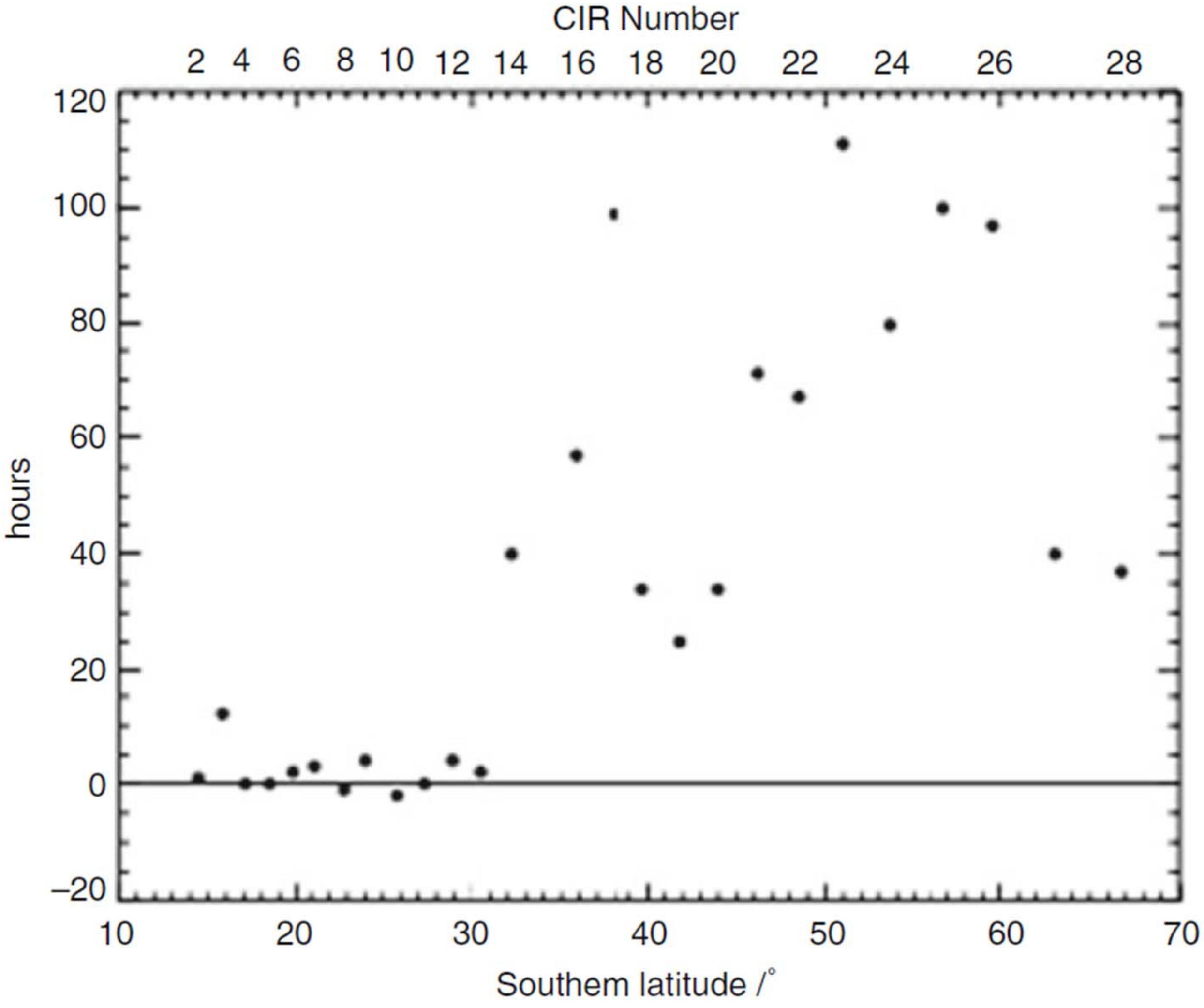

From CIR 2–13, essentially no lags were observed, whereas for the later CIRs lags from 1–4 days were normal. We were fortunate in 1992–1996 to be confident that the main source of the near-relativistic electrons detected at Ulysses was the reverse shock from the long-lived CIR.

The difference in time between the 12 h mean maxima of 1MeV/amu ions and relativistic electrons. Positive times correspond to ions arriving first.

Fig. 6.6 (p.129) in Simnett et al. (2017)

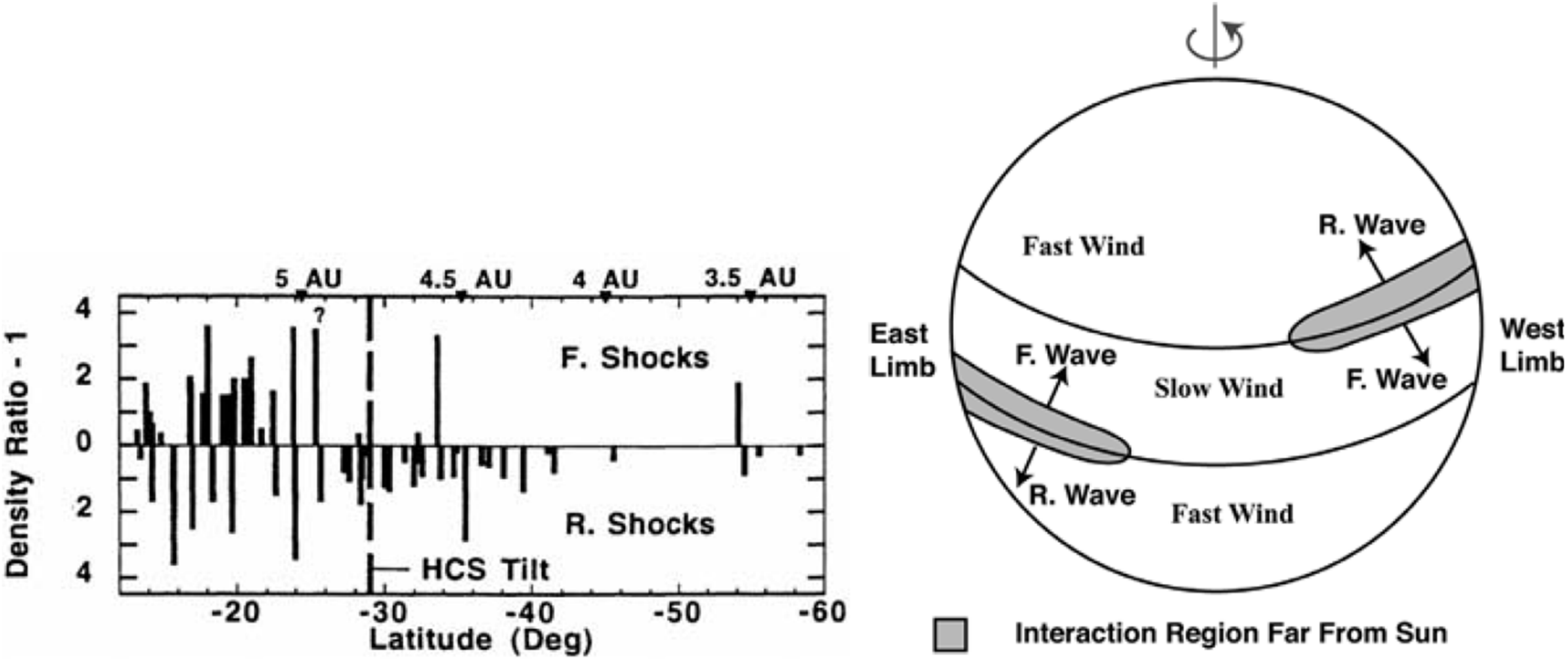

Fig. 3.13 (p.63) in Balogh et al. (2008)

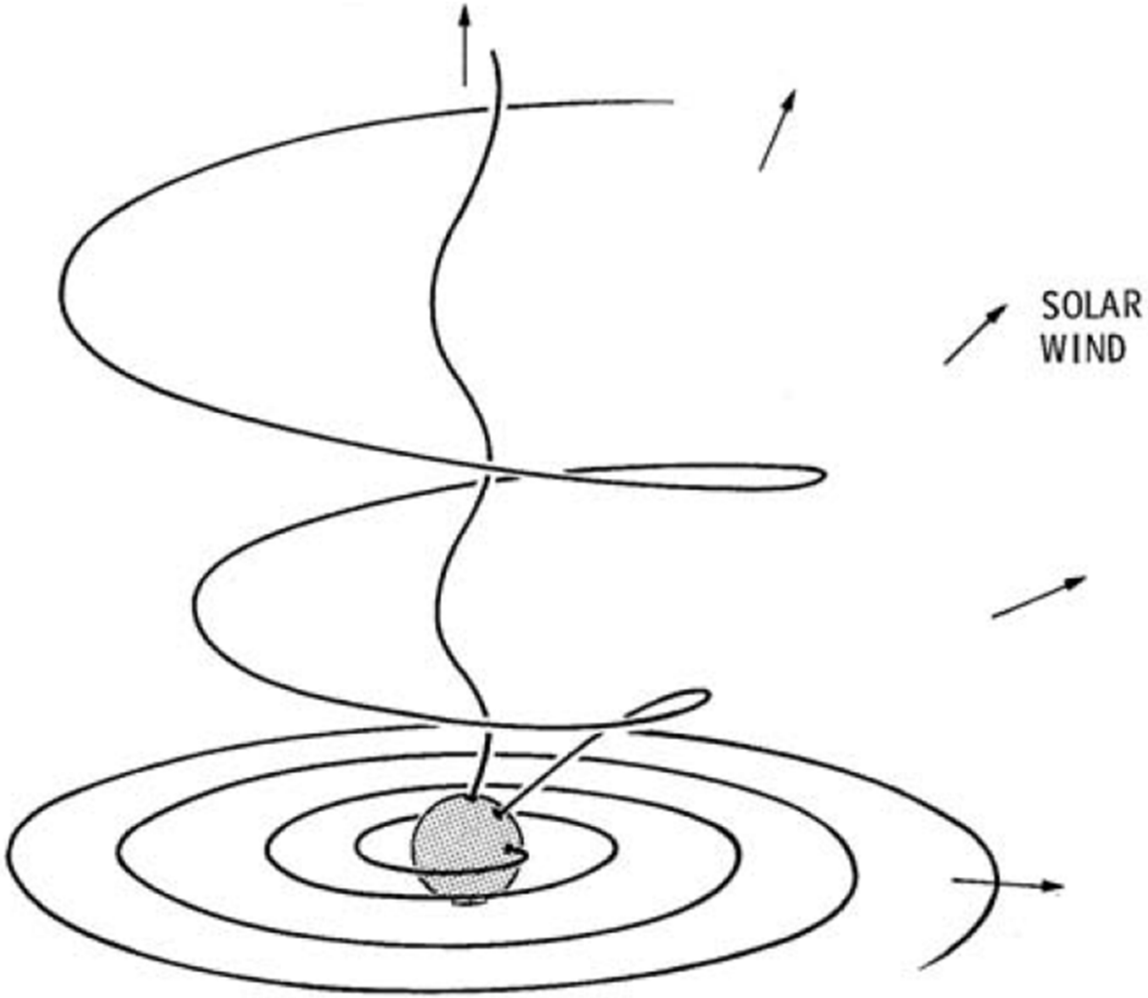

Fig. 4.2 (p.83) in Balogh et al. (2008)

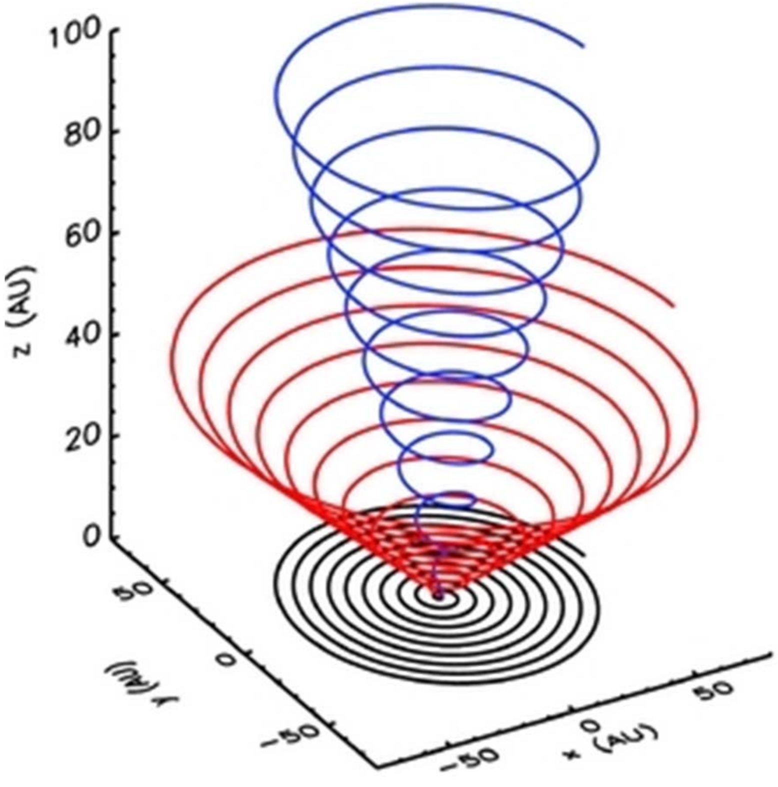

http://iopscience.iop.org/article/10.1088/0004-637X/741/1/23

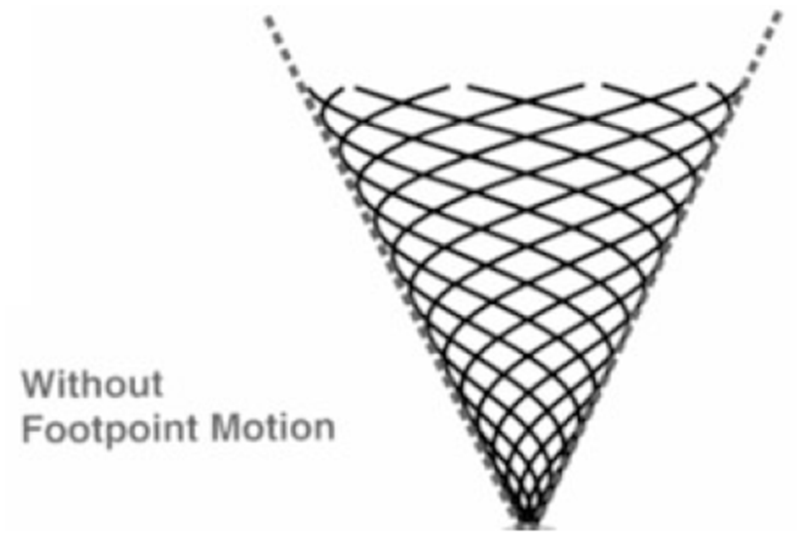

Fig. 6.12 (p.134) in Simnett et al. (2017)

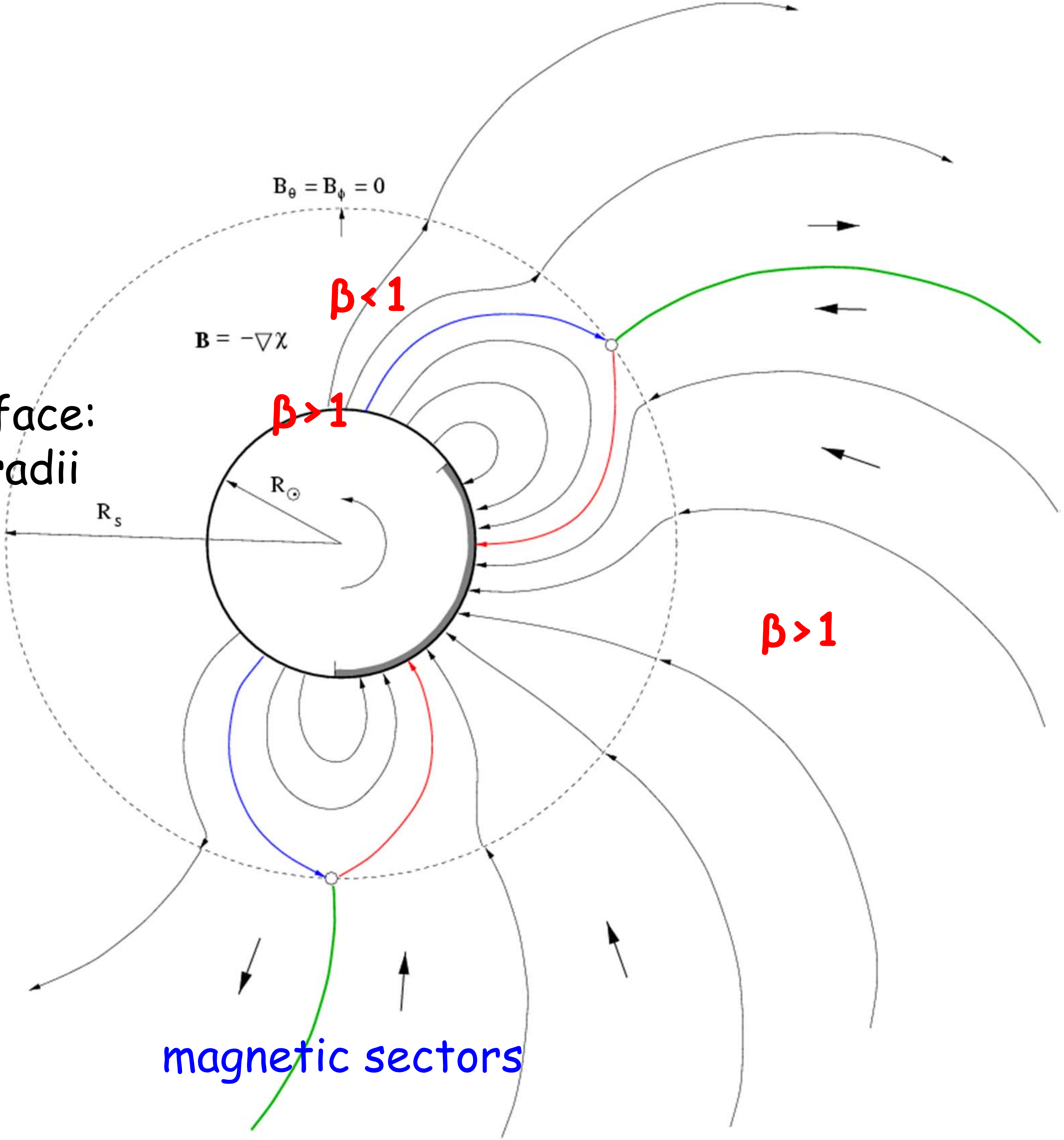

source surface:
2.5 solar radii

$\beta < 1$

$\beta > 1$

$\beta > 1$

magnetic sectors

http://sprg.ssl.berkeley.edu/~tohban/nuggets/?page=article&article_id=29

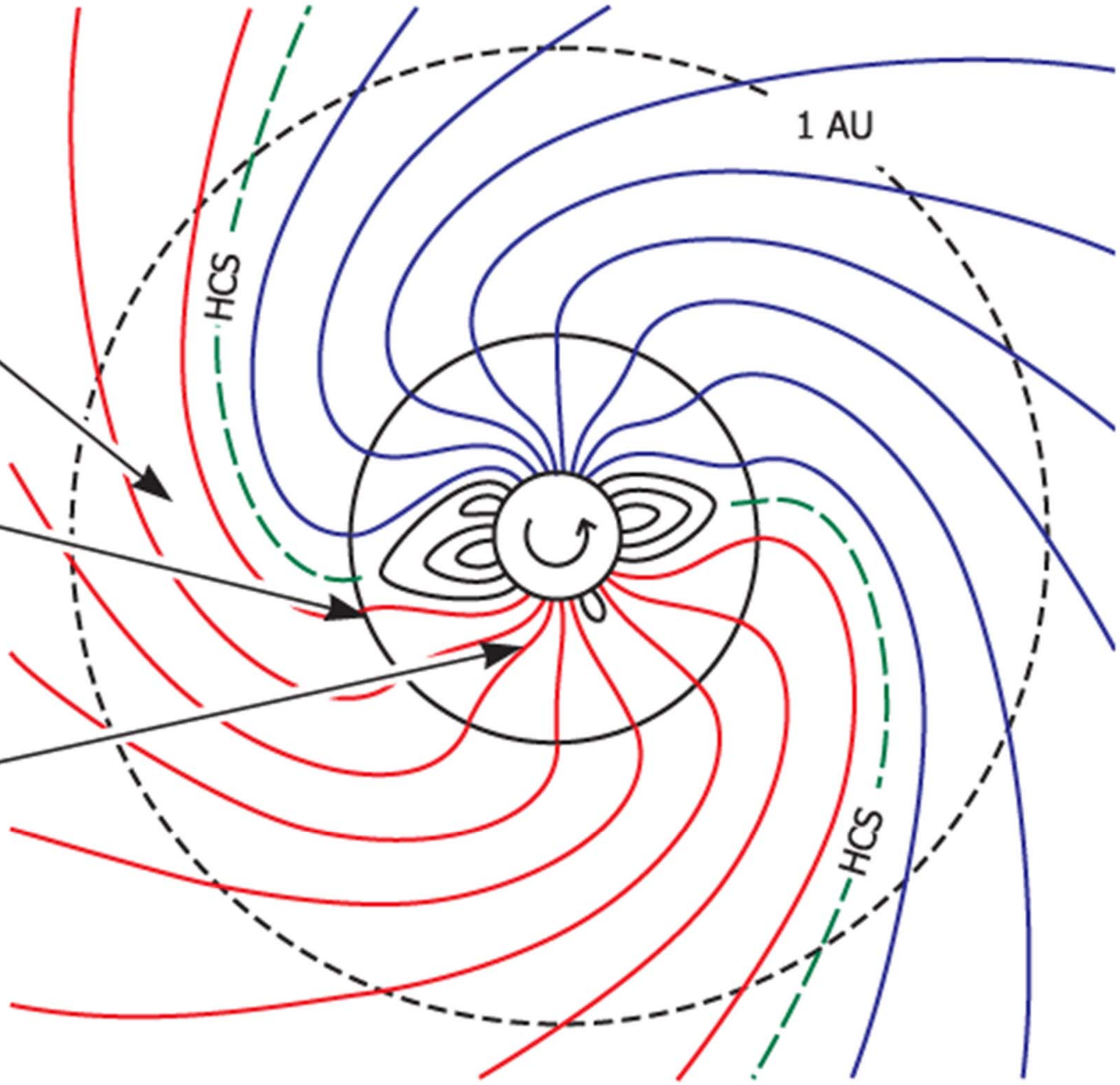

Heliosphere

$\vec{B} = B_R\,\hat{R} + B_\phi\,\hat{\phi}$

$\vec{V} = V_R\,\hat{R}$

Source surface

$\vec{B} = B_R\,\hat{R}$

$\vec{V} = V_R\,\hat{R}$

Super-radial expansion

$\vec{B} = B_R\,\hat{R} + B_\theta\,\hat{\theta} + B_\phi\,\hat{\phi}$

$\vec{V} = V_R\,\hat{R} + V_\theta\,\hat{\theta} + V_\phi\,\hat{\phi}$

http://solarphysics.livingreviews.org/Articles/lrsp-2013-5/fig_1.html

There are three basic assumptions in the model of Fisk (1996) :

1. The heliospheric magnetic Field is attached to the photosphere, which differentially rotates.
2. The high-speed solar wind expands nonradially from polar coronal holes.
3. The expansion of the solar wind in the polar coronal holes is about an axis that is offset from the solar rotation axis and that also tends to rotate rigidly at approximately the equatorial rotation rate.

→ lead to large excursions in latitude of the heliospheric magnetic field

p.132 in Simnett et al. (2017)

Fisk et al. (1999)

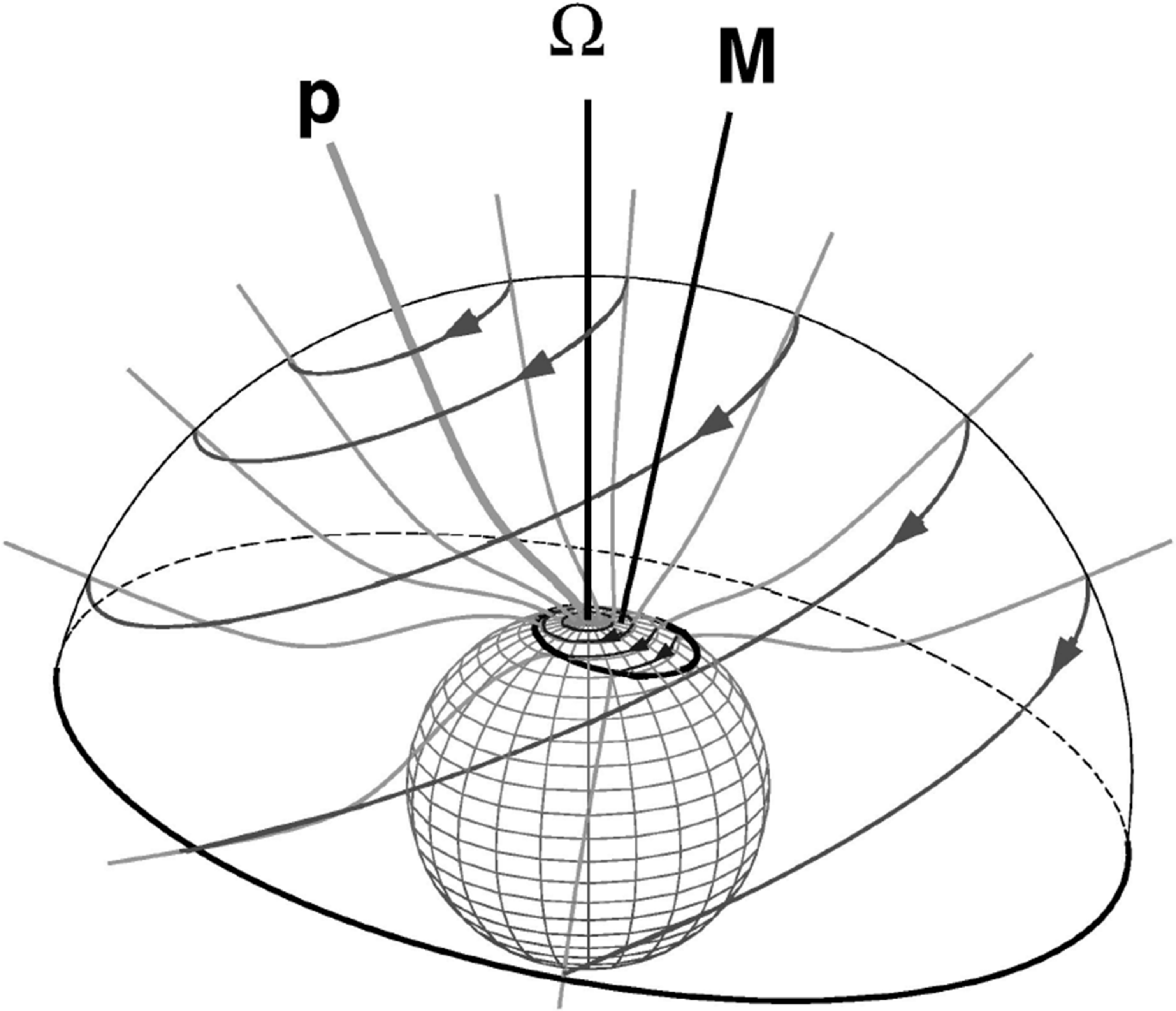

The magnetic field line coming from the magnetic pole **p** undergoes a non-radial expansion about the dipole axis **M** and emerges into the solar corona. All the field lines are anchored in the differentially-rotating photosphere and they therefore execute circular motion about Ω, which following the non-radial expansion from the north-polar coronal hole, results in distorted circular motion about **p**. The circles on the imaginary hemispherical surface then make large excursions in heliospheric latitude.

FIG. 1.—An illustration of the motions of the magnetic field in the corona, in the polar coronal hole, as predicted by the model of Fisk (1996, after Zurbuchen et al. 1997). The outer surface, which is defined in the text, is penetrated only by field lines which open into the heliosphere and which have essentially constant magnetic pressure. The figure is drawn in the frame corotating with the equatorial rotation rate. The M-axis is the axis of symmetry for the expansion of the magnetic field from a polar coronal hole. The Ω-axis is the solar rotation axis. The open lines are field lines, with p marking the field line that connects to the solar pole. The curves with arrows are the trajectories of the field lines, the motion of which is driven by differential rotation of the photosphere.

Fisk et al. (1999)

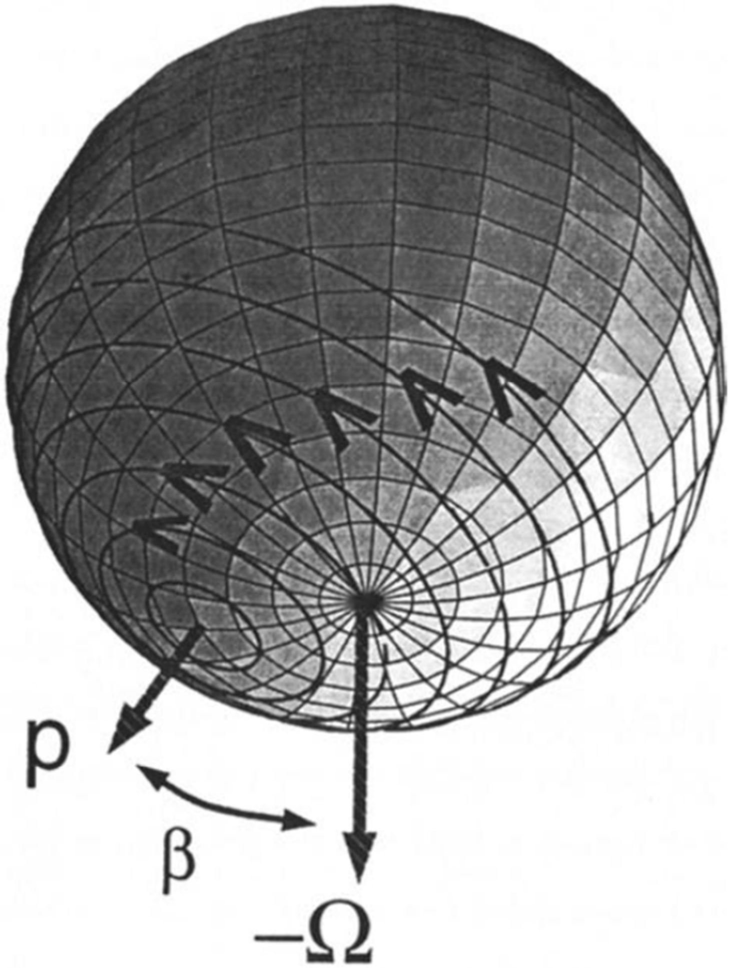

Figure 2. The southern hemisphere of the solar wind source surface drawn in the frame corotating with the equatorial rotation rate. The trajectories of the heliospheric magnetic field lines execute circular patterns moving in heliographic latitude and longitude.

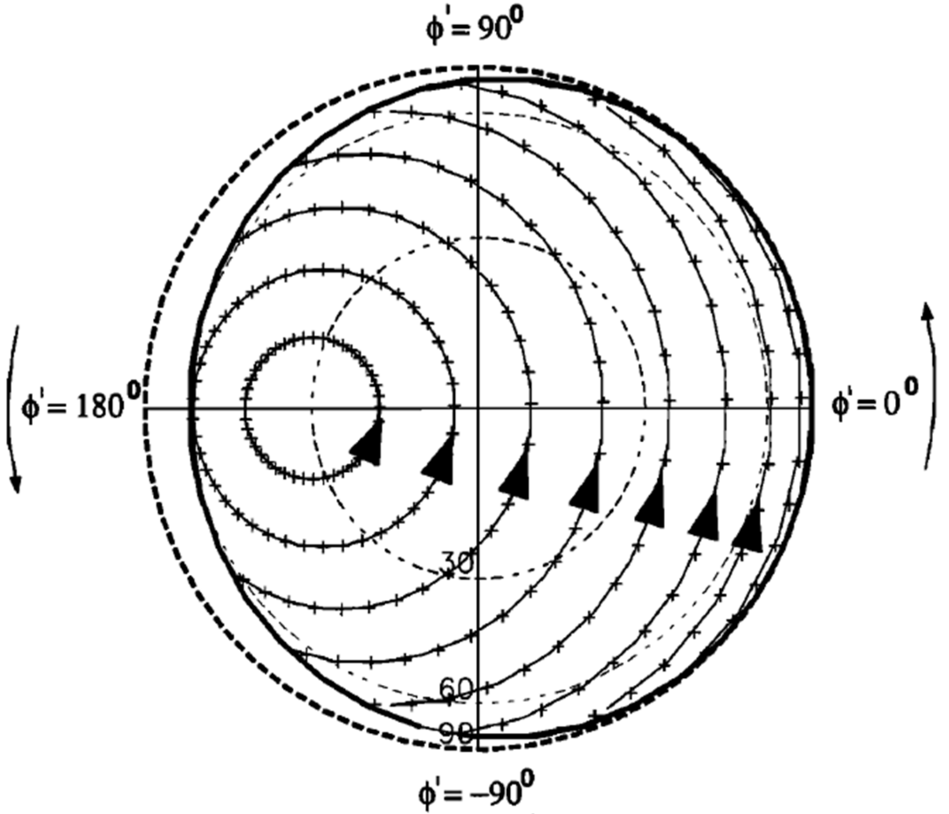

Figure 3. The trajectories of the footpoints of the heliospheric magnetic field lines on the solar wind source surface, projected onto the equatorial plane. The trajectories are shown in the frame corotating at the equatorial rotation rate of the sun; the perspective is from the south solar pole. The solar wind in this frame flows counterclockwise as indicated by the arrows outside the figure. The footpoints of the field lines move in the directions indicated by the arrows on the trajectories. The rate of motion of the footpoints is indicated by the markers on the trajectories which are spaced at intervals equal to the distance a footpoint will move at a rate given by (2) and during a time interval equal to the transit time of fast solar wind over 1 AU (2.2 days). The footpoint trajectories end when the footpoint of the field line in the photosphere encounters the coronal hole boundary.

Zurbuche et al. (1997)

Fisk (1996)

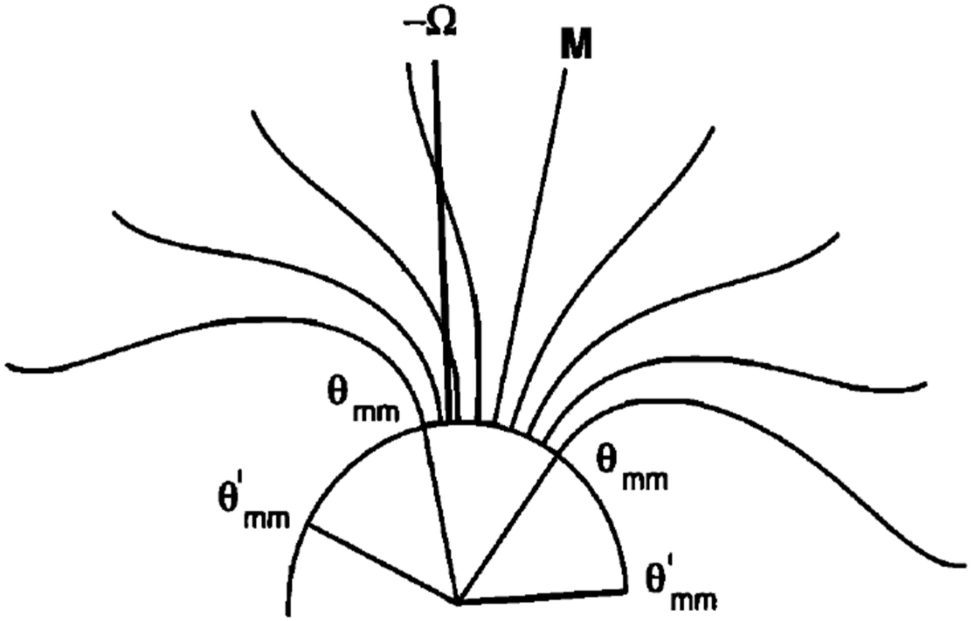

Figure 2. A schematic illustration of the expansion of magnetic field lines from a polar coronal hole.

Fisk (1996)

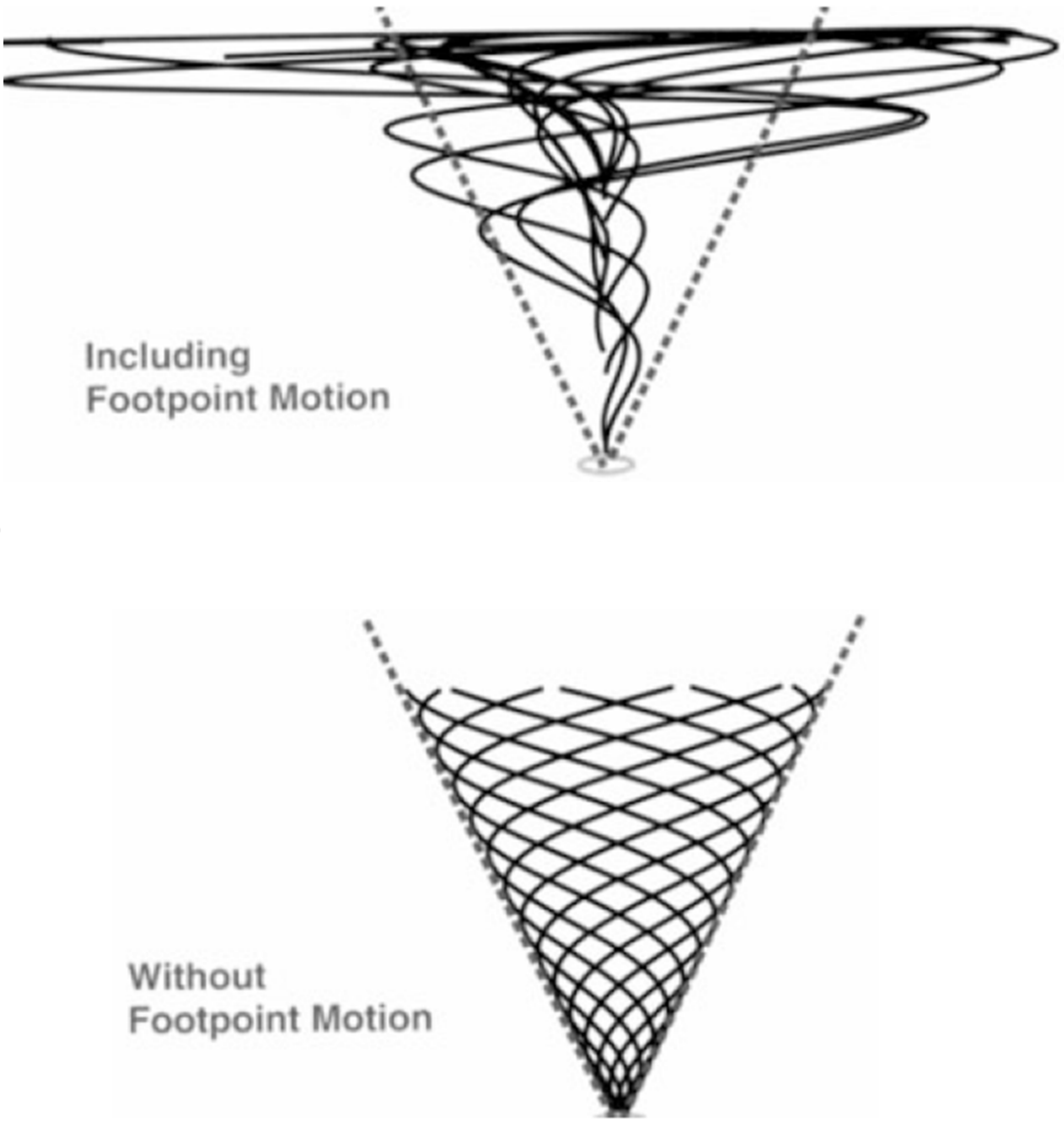

Fig. 6.12 (p.134) in Simnett et al. (2017)

The Fisk model leads to equations for the field components that differ significantly from the Parker equations:

$$B_R = B_o\left(\frac{r_o}{r}\right)^2$$

$$B_\theta = \left(\frac{B_o r_o^2}{r V_R}\right)\omega \sin\beta \sin\left(\phi + \frac{\Omega r}{V_R} - \phi_o\right)$$

$$B_\phi = \left(\frac{B_o r_o^2}{r V_R}\right)\left[\omega\left(\cos\beta\sin\theta + \sin\beta\cos\theta\left(\phi + \frac{\Omega r}{V_R} - \phi_o\right)\right) - \Omega\sin\theta\right]$$

The field strength at the source surface located at r_0 is B_0. The co-latitude and longitude in heliographic coordinates are θ and ϕ, and ϕ_o is the longitude of the magnetic pole. The differential rate of rotation, $\omega = \Omega - \Omega(\theta)$—that is, the difference between the angular velocity at the equator and at high latitudes (not the angular velocity at high latitudes).

When $\beta = 0$, the equations reduce to the Parker equations:

$$B_\theta = 0$$

$$B_\phi = \left(\frac{B_o r_o^2}{r V_R}\right)[(\omega - \Omega)\sin\theta]$$

p.113 & 114 in Balogh et al. (2008)